https://doi.org/10.5194/egusphere-2025-6492
Preprint. Discussion started: 23 March 2026

Elevated foehn exacerbates surface ozone pollution in summer Beijing

Zhiheng Liao[1], Jing Xu[1], Ju Li[1], Liyan Zhou[1], Chao Liu[1], Lin Wu[2], Zhiqiang Ma[1]

[1]Institute of Urban Meteorology, China Meteorological Administration, Beijing, China;
[2]Huairou Meteorological Office of Beijing, Beijing, China.

Correspondence: Z. Liao (zhliao@ium.cn) and Z. Ma (zqma@ium.cn)

Abstract: While several studies have evaluated the impact of shallow foehn on air pollution, the effects of elevated foehn on O_3 pollution remain poorly understood. Here, we investigate the role of elevated foehn in summer O_3 pollution in Beijing through detailed case analysis and a long-term climatological evaluation. The case study reveals that elevated foehn exacerbates next-day O_3 pollution through three primary mechanisms: first, by increasing boundary layer temperature, thereby enhancing photochemical O_3 formation; second, by reducing the residual/boundary layer height, thereby inhibiting vertical diffusion of pollutants; and third, by slowing boundary layer winds, thereby suppressing horizontal dispersion. A ten-year climatological evaluation of 54 identified elevated foehn events strongly supports these mechanisms. On average, these events led to a post-foehn afternoon boundary layer temperature increase exceeding 3°C, an afternoon boundary layer height reduction of more than 100 m, and a decrease in afternoon boundary layer wind speed of more than 1.0 m s^{-1} compared to the pre-foehn days. Consequently, 87% of elevated foehn events were associated with a worsening of O_3 pollution. Post-foehn daily maximum 8-hour average O_3 concentrations frequently surpassed the national pollution threshold (160 μg m^{-3}), with an average increase of 20%–60% (varying by site and higher in urban areas) compared to preceding days. These results demonstrate a robust and deterministic exacerbating effect of elevated foehn on surface O_3 pollution, suggesting that elevated foehn can serve as a reliable meteorological precursor for O_3 pollution warnings in summer Beijing.

Keywords: elevated foehn, atmospheric boundary layer, residual layer warming, ozone pollution, Beijing

1. Introduction

Foehn is a phenomenon of downslope winds with significant warming on the mountain leeside (Elvidge and Renfrew, 2016). It has been observed among many large mountains in the world, including the Alpine Mountains (Miltenberger et al., 2016; Seibert et al., 2000), Rocky Mountains (Kerr, 1986), Appalachian Mountains (Gaffin, 2002, 2009), Taihang Mountains (Li et al., 2020a; Li et al., 2025), and Tianshan Mountains (Li et al., 2015; Li et al., 2020b). The societal and economic impacts of foehn winds are wide-ranging and well-documented, encompassing enhanced fire risks, extreme heat exposure, impacts on air quality, beneficial impacts on agriculture, and direct wind-driven damage to infrastructure. Given these multifaceted impacts, foehn has long been a subject of sustained scholarly interest across diverse disciplines.

Scientific research into the effect of foehn on air pollution began in in Europe in the late nineteenth century, primarily to explain elevated ozone (O_3) levels in the Alpine regions during foehn events (Baumann et al., 2001; Campana et al., 2005; Seibert et al., 2000). Early European studies identified that the initial rise in O_3 concentration was caused by the advection of residual-layer air masses from source regions such as the Po Basin. Later on, O_3 levels in the foehn-affected area were found to be influenced by regional-scale advection from the lower free troposphere or even the stratosphere. Collectively, these studies emphasized the transport role of foehn in influencing O_3 air quality in the relatively clean valleys of Alps. In contrast, research in China has commonly demonstrated a “clearance effect” of foehn on air pollution in highly-polluted cities (Li et al., 2020a; Li et al., 2025; Yang et al., 2018). For example, Yang et al. (2018) reported a case in Shijiazhuang where foehn led to rapidly improved horizontal visibility, decreased aerosol concentration, and weakened haze intensity. Similarly, a six-year statistical study by Li et al. (2025) found that 60.4 % of foehn events were associated with a subsequent decrease in fine particulate matter ($PM_{2.5}$) concentrations in Beijing. This clearance effect is attributed to the origin of the foehn winds, which typically transport cleaner air from the less polluted western, northwestern and northern mountain areas of the Hebei–Beijing region into more polluted plains.

These abovementioned studies, conducted in both Europe and China, primarily examine the foehn effect on air pollution mainly from a dynamical (transport) perspective. Furthermore, the foehn cases selected in these studies are generally confined to shallow foehns, identifying using near-surface meteorological observations. Crucially, however, the defining feature of foehn is the associated warming (Elvidge and Renfrew, 2016). This warming inevitably alters the vertical thermal structure—and thus the atmospheric stability—which directly governs the capacity for vertical diffusion of air pollutants (Liao et al., 2018; Stull, 1988). Therefore, the vertical extent of the foehn (shallow or elevated) critically determines its impact on atmospheric stability: shallow foehn tends to enhance near-surface instability, while elevated foehn can strengthen stability within or above the boundary layer. From this thermodynamic perspective, elevated foehn likely possesses a greater pollution potential than its shallow counterpart. Despite this reasoning, to the best of our knowledge, only one study—Li et al. (2015) in Urumqi, a city adjacent to Tianshan Mountains—has explicitly investigated the impact of an elevated foehn on air pollution from a thermodynamic viewpoint. That study revealed that an elevated southeasterly foehn layer between 480 and 2100 m created a very stable boundary layer structure, which suppressed vertical mixing and led to severe haze pollution episodes. Recent studies on $PM_{2.5}$ pollution in Beijing (Li et al., 2020a; Li et al., 2025) have speculated that post-foehn pollution exacerbation might be driven by a mechanism similar to the elevated foehn process observed in Urumqi (Li et al., 2015). However, the existence and role of such an elevated foehn mechanism have not yet been observationally confirmed for Beijing.

Beijing, the capital of China, faces significant challenges in terms of air pollution. Particularly in recent summers, O_3 has surpassed $PM_{2.5}$ as the most important air pollutant, arousing widespread attention (Liao et al., 2023; Zong et al., 2023). The city’s location on the plains adjacent to the Taihang Mountains to the west and the Yan Mountains to the north makes it particularly susceptible to foehn winds. Luo et al. (2020) documented an intensive foehn warming event in Beijing where nocturnal air temperatures increased by over 10℃ per hour. Utilizing data from a density automatic weather station network, Li et al. (2025) developed a foehn identification method and reported an annual average of 56.5 foehn days in Beijing. As noted earlier, their statistical analysis suggests a higher probability of $PM_{2.5}$ pollution alleviation (60.4 %) rather than pollution exacerbation (39.6 %) following foehn events in Beijing. Importantly, because their identification method only relies on near-surface observations, the detected events are predominantly shallow foehns. This methodological focus may obscure the distinct air pollution effects potentially caused by elevated foehns. Therefore, determining whether elevated foehn induces a more deterministic—and likely adverse—pollution effects is a critical unanswered question. The answer has practical importance, as it would inform whether elevated foehn can serve as a reliable precursor indicator for air pollution warnings, thereby improving mitigation efforts in Beijing and other leeside cities.

To address this knowledge gap, our team deployed two O_3 lidars at an urban (Guanxiangtai, GXT) and a rural (Shangdianzi, SDZ) station in Beijing in late July 2024. This coordinated dual-station lidar setup is particularly

https://doi.org/10.5194/egusphere-2025-6492
Preprint. Discussion started: 23 March 2026

suited to capturing the three-dimensional characteristics and mechanisms of boundary layer O_3 evolution under the influence of elevated foehn. One month after deployment (27–31 August), we observed an O_3 pollution episode associated with an elevated foehn. In this study, we conducted a detailed analysis of this event by integrating data from the new lidar system with co-located remote sensing meteorological observations. We supplement this case study with a climatological evaluation using a decade (2015–2024) of routine observations. Our overarching aim is to elucidate the specific role of elevated foehn in driving summer O_3 pollution in Beijing.

2. Data and method

2.1. Observational data

Figure 1 shows the observation network and instruments. The network comprises 3 meteorological stations and 46 surface O_3 monitoring sites. Among the O_3 sites, 45 are air quality stations operated by the Beijing Municipal Ecological and Environmental Monitoring Center, and one is the Shangdianzi (SDZ) atmospheric background station managed by the Beijing Meteorological Bureau. Two differential absorption O_3 lidars (Hefei GBQ Technology Company) were deployed at the GXT (urban) and SDZ (rural) stations, respectively. These lidars measured O_3 profiles with a 5-minute resolution up to an altitude of 3.0 km. In addition, radar wind profilers at GXT, SDZ, as well as Yanqing (YQ) provided continuous wind profiles at 6-minute resolution. Routine meteorological radiosondes launched from the GXT station provided high-vertical-resolution (~10 m) profiles of temperature, relative humidity, wind speed, and wind direction three times daily (08:00, 14:00, and 20:00 BJT) in summer.

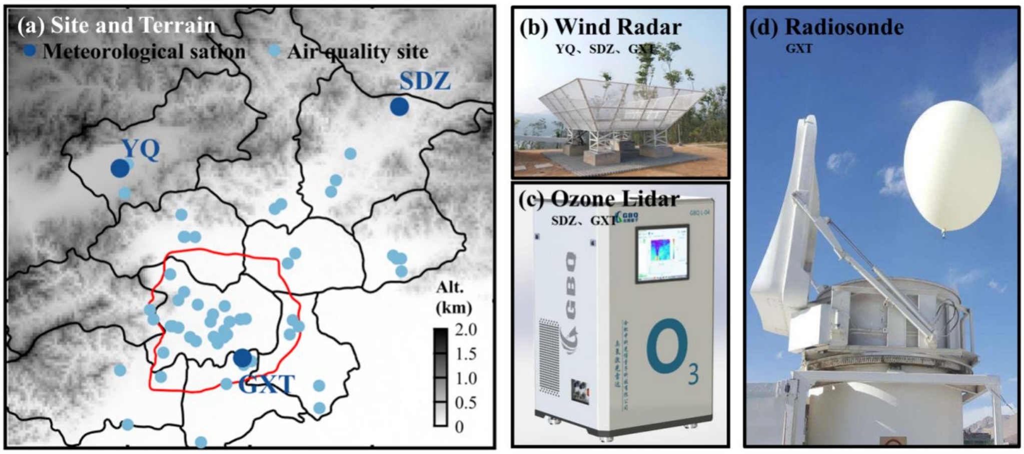

Figure 1. Site distribution of surface ozone and meteorological measurements, and ground-based remote sensing instruments used in this study. In (a), dark blue dots denote the GXT, SDZ, and YQ meteorological stations; light blue dots represent the surface ozone observation sites. Panels (b), (c), and (d) show the radar wind profilers at YQ, SDZ, and GXT, ozone lidars at SDZ and GXT, and routine radiosonde instrument at GXT, respectively.

To validate the lidar O_3 observations, we compared the lidar-derived O_3 concentration at 300 m height (the lowest reliable altitude above the instrument's blind zone) with surface measurements. As no surface O_3 data were available at the GXT site, we used measurements from the nearest air quality monitoring station (~2 km away). The validation results demonstrated a strong correlation between the lidar-based and surface-based O_3 concentrations (R^2 = 0.69 at GXT and R^2 = 0.56 at SDZ), confirming the reliability of the O_3 lidar data (Fig. S1). To construct complete vertical profiles for calculating O_3 transport flux, we used linear interpolation between the surface O_3 measurement and the validated lidar observation at 300 m to fill the blind zone. A similar procedure was applied to patch the blind zone (below 150 m) of the radar wind profiler data, where winds were interpolated between the surface wind observation and the lowest valid radar measurement at 150 m.

2.2. Identification of elevated feohn

To date, no established method exists for identifying elevated foehn. For the purpose of climatological evaluation, we develop a framework (Fig. 2) to identify elevated foehn events based on the combination of meteorological radiosonde data and a Lagrangian trajectory model. First, we calculated overnight temperature change (ΔT_{12h}) profiles by subtracting the radiosonde temperature profiles at 20:00 BJT (sunset) from the profiles at 08:00 BJT the following day (sunrise) on a night-by-night basis (i.e., $\Delta T_{12h}=T_{08}-T_{20}$). A residual layer warming event was identified when $\Delta T_{12h}>3$℃ occurred within 500-2000 m AGL layer. This threshold is also commonly used to identify ground-based foehn elsewhere (Kirchgaessner et al., 2021; Steinhoff et al., 2014). Finally, we examined the backward trajectory properties (including geographic origin, height change, and temperature change) of the air mass at the identified maximum warming height (i.e., the height of maximum ΔT_{12h}) using a Lagrangian trajectory model (Miltenberger et al., 2016). If the 12-h backward trajectory originated from the mountains (azimuth of 250–360^o or 0–45^o, following Li et al. (2025)), and if the trajectory descended more than 300 m accompanied by a temperature increase exceeding 3 ℃ before arriving in Beijing, we attribute the identified warming case to an elevated foehn event.

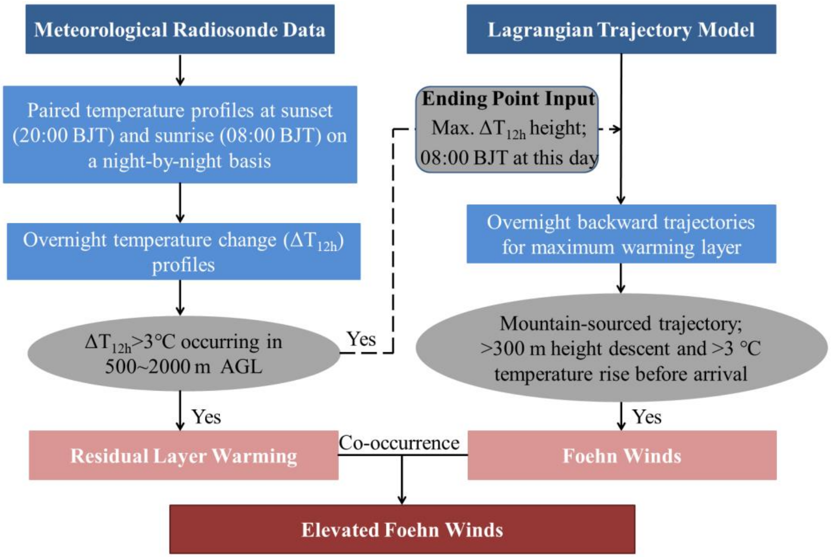

Figure 2. Flowchart for identifying elevated foehn based on the combination of meteorological radiosonde data and a Lagrangian trajectory model.

2.3. Supporting calculations and model simulations

The boundary layer structure during a diurnal cycle can be classified into three regimes: convective boundary layer (CBL), stable boundary layer (SBL), and residual layer (RL) (Stull, 1988). We determined the boundary layer height based on high-resolution radiosonde profiles from the GXT station. Following Liu and Liang (2010), the height of the CBL (CBLH, at 14:00 BJT) was determined at the base of the overlying temperature inversion capping the convective thermals. The height of the SBL (SBLH, at 20:00 and 08:00 BJT) was determined at the top of the underlying temperature inversion, where turbulence nearly ceases. At the morning transition (08:00 BJT), emerging solar radiation gradually erodes the near-surface part of the SBL; thus, the SBLH at this time was determined at the top of the residual underlying temperature inversion. The RL is disconnected from the ground by the underlying SBL but retains the atmospheric state of the former CBL. Its height (RLH) was therefore determined at the base of the overlying temperature inversion at the evening or morning transition (20:00 and 08:00 BJT). For temperature profiles showing no significant overlying inversion, the CHLH and RLH were determined using a multi-variable integrated method proposed by Wang and Wang (2014).

To analyze O_3 transport in Beijing, we calculated the O_3 transport flux (TF) using collocated wind and O_3 profiles from the GXT and SDZ sites. The transport flux (TF, mg m^{-2} s^{-1}), representing the mass flow per unit cross-sectional area per unit time, is determined by the wind speed and the O_3 concentration. The TF at a certain height and direction is calculated as follow:

$$TF = C \times WS \times \cos\left[(WD - B) \times \frac{\Pi}{180}\right]$$

where C represents the O_3 concentration (unit: μg m^{-3}), WS denotes the horizontal wind speed (unit: m s^{-1}), WD denotes the horizontal wind direction and B is the azimuth from the start station to the end station. In this study, we calculated O_3 transport flux in the direction from GXT to SDZ. Therefore, positive TF indicates northeastward transport, and negative TF indicates southwestward transport.

We used the Hybrid Single-Particle Lagrangian Integrated Trajectory (HYSPLIT) model (Stein et al., 2015) to trace the origin and history of the air masses associated with the maximum residual layer warming in Beijing. In addition to HYSPLIT, we employed the Weather Research and Forecasting model with Chemistry (WRF-Chem, version 4.2.1) to simulate O_3 concentrations and meteorological fields. The WRF-Chem model accounts for key atmospheric processes, including emissions, deposition, advection, diffusion, gas-phase chemistry, and aerosol chemistry (Grell et al., 2005). Our simulation domain encompassed most of China, centered at (105.5 °E, 37.5 °N), with a horizontal grid spacing of 9 km. The meteorological initial and boundary conditions were derived from the National Centers for Environmental Prediction (NCEP) Final Operational Global Analysis data. For emissions, we utilized the Model of Emissions of Gases and Aerosols from Nature (MEGAN) (Guenther et al., 2006) and the Multi-resolution Emission Inventory for China (MEIC) (Zhang et al., 2009), with the latter updated to a 0.1 ° × 0.1 ° resolution for 2019 (MEIC-2019; http://www.meicmodel.org). The detailed model configuration follows Xu et al. (2024). The WRF-Chem simulation demonstrated a reasonable agreement with observed surface O_3 concentrations during the studied pollution episode ($R^2 = 0.51$ at GXT and $R^2 = 0.44$ at SDZ; Fig. S2).

3. Results

3.1. Case study

3.1.1. Overview of the O_3 pollution episode

Following heavy rainfall on 26 August 2024, Beijing experienced consecutive sunny days until light rain resumed on 31 August. The persistent sunny weather established favorable meteorological background for photochemical O_3 production. Consequently, surface O_3 concentrations in Beijing exhibited a daily increasing trend from 27 to 30 August. On the final two days (29 and 30 August), the city-averaged daily maximum 8-hour average O_3 (MDA8O_3) concentrations approached or exceeded China's ambient air quality standard threshold of 160 μg m^{-3}, peaking at 174 μg m^{-3} on 30 August (Fig. 3a). A notable feature of these two polluted days was the stark contrast in the spatial distribution of O_3 concentrations. On 29 August, the spatial pattern showed a positive O_3 gradient

https://doi.org/10.5194/egusphere-2025-6492
Preprint. Discussion started: 23 March 2026

extending northeastward, which was reversed on 30 August (Fig. 3b, c). This contrast was exemplified by the station observations: SDZ recorded its peak O_3 concentration (212 µg m^{-3} at 18:00 BJT) on 29 August, significantly higher than the concurrent value at GXT (161 µg m^{-3}). Conversely, GXT observed its maximum O_3 level (249 µg m^{-3} at 16:00 BJT) on 30 August, far exceeding the measurement at SDZ (138 µg m^{-3}; Fig. 3a). These contrasting spatial patterns seem to represent two typical O_3 pollution scenarios in Beijing: an urban plume transport pattern and an urban pollution accumulation pattern, as previously reported by Zong et al. (2023). The key question is what mechanism drove the rapid intensification of O_3 pollution and the reversal of its spatial pattern over the two consecutive days.

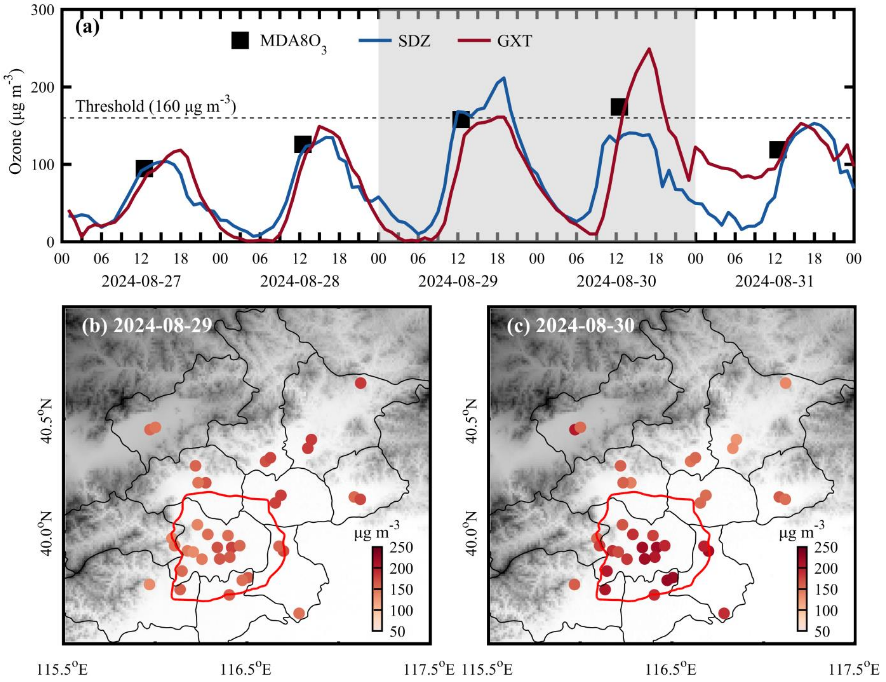

Figure 3. (a) Time series of surface ozone concentrations at the GXT and SDZ stations from 27 to 31 August 2024; Spatial distribution of maximum 8-h O_3 concentrations over Beijing on (b) 29 and (c) 30 August. In (a), black squares represent the city-averaged $MDA8O_3$ concentrations; gray shading denotes the two polluted days (29 and 30 August 2024).

3.1.2. Meteorological attribution to elevated foehn

The weather charts at 08:00 BJT on 29 and 30 August are presented in Fig. 4. A subtropical high prevailed in the upper atmosphere over the central and eastern China, while a typhoon was active over the western Pacific Ocean south of Japan. The coexistence of these two synoptic systems induced widespread clear skies over the eastern China, a condition highly conducive to photochemical O_3 production (Ouyang et al., 2022; Shu et al., 2016). In the lower atmosphere, the synoptic patterns differed between the two days. On 29 August, the North China Plain (NCP) was under the influence of a weak high-pressure system. By 30 August, another high-pressure system (a cold front) had intruded into the northwestern NCP from the Mongolian Plateau, creating a strong pressure gradient perpendicular to the Taihang Mountains. Traditionally, cold fronts are known to have a significant clearance effect on air pollutants (Zhang et al., 2021). However, in this case, the cold front led to an unexpected O_3 increase in

Beijing on 30 August. So, what underlying mechanism was responsible for this phenomenon?

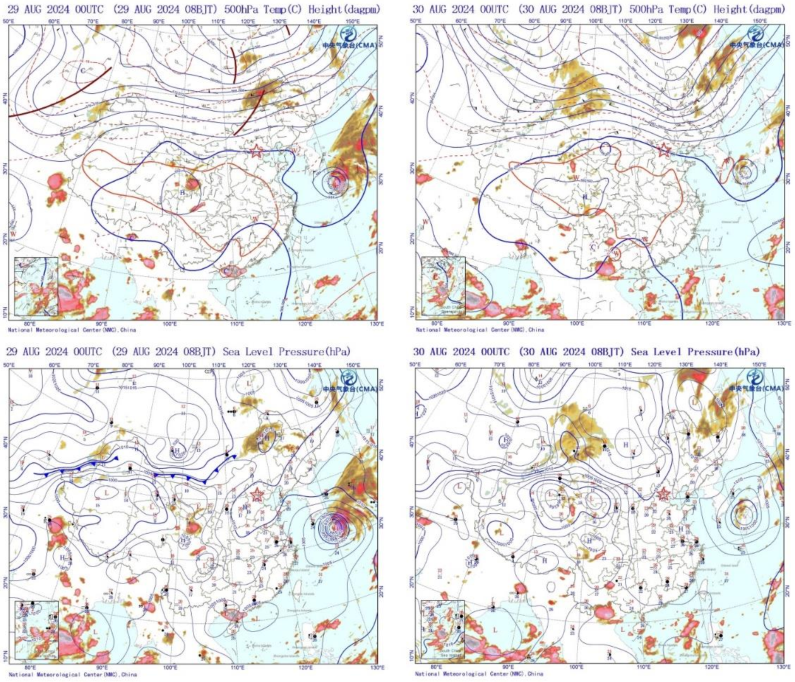

Figure 4. Weather charts at 500 hPa and sea-level pressure over the East Asia at 08:00 BJT on 29 and 30 August, 2024. Shaded areas denote the cloud cover. The location of Beijing is marked by a red star.

To address the question above, we examined the radiosonde profiles and derived boundary layer heights at the GXT station (Fig. 5). The results indicate that the CBLH and RLH on 30 August (750, 880, and 1090 m at 08:00, 14:00, and 20:00 BJT, respectively) were significantly lower than those on 29 August (1300, 1380, and 1260 m at the same times), despite the SBLH showing no significant difference. The CBLH defines the available volume that the pollutants emitted/produced near the surface can occupy, directly affecting their surface concentration and air quality (Tang et al., 2016). Evidently, the significant decline in CBLH contributes to the surface O_3 enhancements in urban Beijing on 30 August. Notably, the two-day CBLH difference originated from a sharp drop (more than 500 m) in RLH between 20:00 BJT on 29 August and 08:00 BJT on 30 August. Comparing radiosonde profiles from these two time points revealed abnormal drying and warming in the residual layer, with a maximum temperature increase of up to 5.8℃ at 1250 m, contrasting sharply with the normal cooling observed the previous night. The base height of this warming layer coincided precisely with the RLH observed at 08:00 BJT on 30 August, indicating that the warming process was responsible for the overnight RLH drop and thereby contributed to the subsequent daytime O_3 pollution exacerbation. Furthermore, the nocturnal residual layer warming inevitably contributes to higher daytime air temperatures. As observed, the afternoon boundary layer temperature on 30 August showed a significant increase compared to the previous afternoon, and this higher temperature further promotes photochemical O_3 production (Gu et al., 2020). That is to say, in addition to promoting daytime O_3 accumulation by reducing the boundary layer height, residual layer warming also enhances the photochemical O_3 production. The remaining question is: what caused the abnormal warming of the nocturnal residual layer under the background of a cold front intrusion?

https://doi.org/10.5194/egusphere-2025-6492
Preprint. Discussion started: 23 March 2026

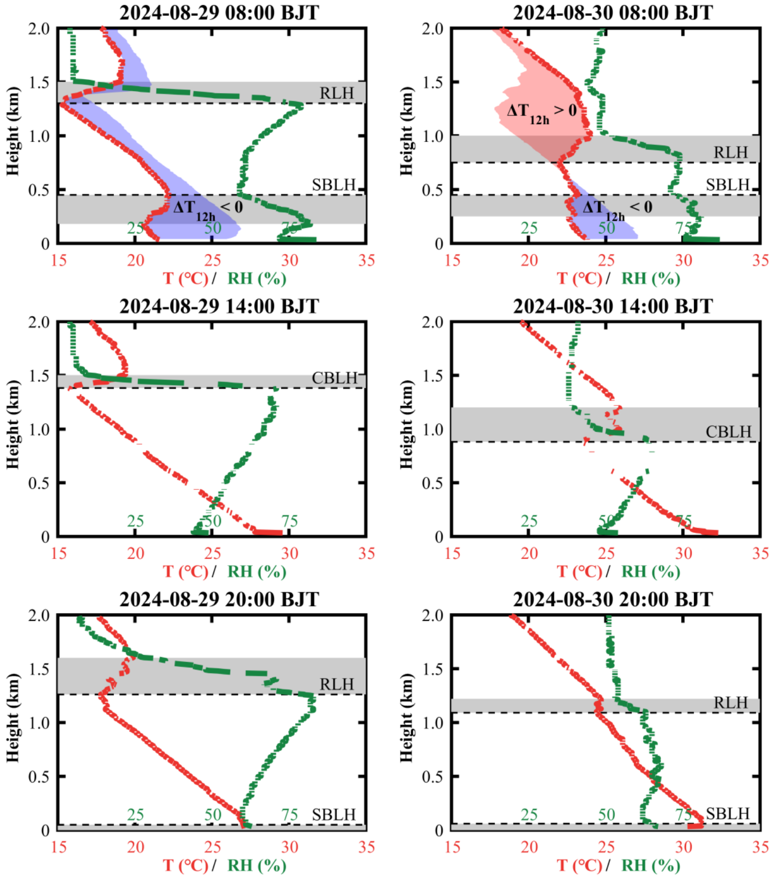

Figure 5. Radiosonde-based temperature (T, red lines) and relative humidity (RH, green lines) profiles at the GXT station. Gray shaded areas represent the heights of temperature inversion layers. Dashed lines denote the afternoon convective boundary layer height (CBLH), and dot lines denote the nocturnal stable boundary layer height (SBLH). Colorful shaded areas highlight the overnight temperature changes, with increase marked in red and decrease in blue. Note: at 08:00 BJT (morning transition), emerging solar radiation collapses the near-surface SBL; thus, the SBLH at this time is determined at the top of the residual underlying temperature inversion.

Using the HYSPLIT model, we traced the 24-hour origin and characteristics of the air mass at the overnight maximum warming height (1250 m) observed at 08:00 BJT on 30 August (Fig. 6b and d). For comparison, we also calculated backward trajectories for the near-surface (150 m) airflow at the same time (Fig. 6b and f), as well as airflows at the same heights and time on the previous day (Fig. 6a, c, and e). The results show that the airflows at 1250 m and 150 m on 29 August, as well as at 150 m on 30 August, all originated from the southern NCP region with no significant change in trajectory height. In contrast, the air mass at the maximum warming height on 30 August originated from the Mongolian Plateau. It moved eastward to the northern side of the Yanshan Mountains, turned southeastward to cross the mountains, and finally arrived in Beijing. During this transport, the airflow first ascended about 1000 m and then descended about 1500 m, accompanied by a temperature change of cooling (7.6℃) followed by warming (11.4℃). These changes in trajectory height and temperature exhibit very pronounced foehn warming characteristics (Elvidge and Renfrew, 2016). Previous studies have reported several cases of shallow foehn-induced nocturnal surface warming in Beijing (Li et al., 2026; Luo et al., 2020). Our case differs significantly because it involves elevated air masses and shows no warming in the surface layer. To confirm this, we examined hourly temperature variations from 20:00 BJT on 29 August to 08:00 BJT on 30 August at 20 surface meteorological stations in Beijing (Fig. S3), as well as at 15 levels on a 325 m high meteorological tower (Fig. S4). The results revealed that, except for the high-altitude Foyeding station (1224.9 m), no temperature surges (ΔT_{1h} >1°C) were observed before sunrise (around 06:00 BJT) at the other stations. This implies no detectable foehn warming signature from standard mountain-leeside surface observations (Li et al., 2025), despite the strong foehn signature in the residual layer. Therefore, we identify this case as the first observation of a novel type of foehn phenomenon in Beijing: elevated foehn in the residual layer.

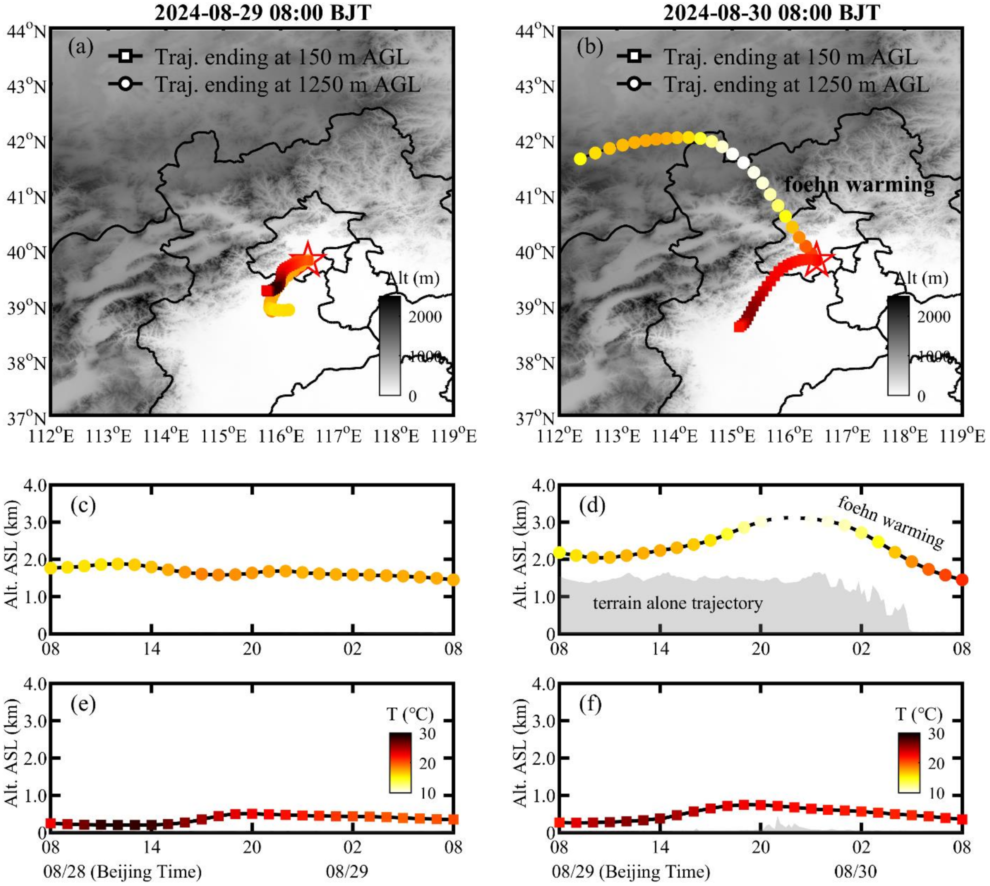

Figure 6. 24-h backward trajectories ending at 150 m (squares) and 1250 m (dots) above ground level (AGL) over the GXT station, at 08:00 BJT of (a) 29 and (b) 30 August. The 1250 m level corresponds to the maximum overnight warming height at 08:00 BJT on 30 August (see Fig. 5). Panels (c-f) show the height and temperature changes of 24-h backward trajectories at 150 and 1250 m. All temperature changes share the same colorbar, including those in (a) and (b).

To illustrate the dynamical conditions during the elevated foehn-induce residual layer warming, Figure 7 presents the radar wind profiles at the YQ, SDZ, and GXT stations from 29 to 30 August. Prior to the warming, southerly winds prevailed in the boundary layer (southwesterly at SDZ and GXT; southeasterly at YQ), while lower free-tropospheric winds gradually shifted from southwesterly to northwesterly. After sunset on 29 August, the cold front intrusion induced strong northeasterly winds in the lower free troposphere at all stations. These northeasterly winds aloft first descended into the boundary layer at YQ, followed by SDZ. In contrast, GXT maintained southwesterly boundary-layer winds until later in the night, forming a distinct northwesterly wind shear zone aloft. During this process, the height of the northwesterly wind shear corresponded well with the sounding-derived RLH at GXT, and the northwesterly winds matched the HYSPLIT backward trajectories ending at GXT (Fig. 6b). Combining the HYSPLIT results, these features strongly support the mechanism of an elevated northwesterly foehn during the residual layer warming period. The elevated foehn appears to have occurred within a shallow wind shear zone, similar to the elevated foehn scenario reported in winter Urumqi by Li et al. (2015). After the residual layer warming, northeasterlies prevailed in the boundary layer at SDZ and southwesterlies at YQ, whereas GXT showed highly variable winds with weak speeds—likely due to convergence between the emerging northwesterly foehn and the prevailing southwesterly flows. This weak-wind stagnant condition suppressed the horizontal dispersion of air pollutants. Operating in conjunction with the inhibited vertical dispersion (from a lower boundary layer height) and accelerated photochemical production (due to higher temperatures), this post-foehn convergent stagnation represent a third contributing factor to the severe daytime O_3 pollution observed in urban Beijing on 30 August.

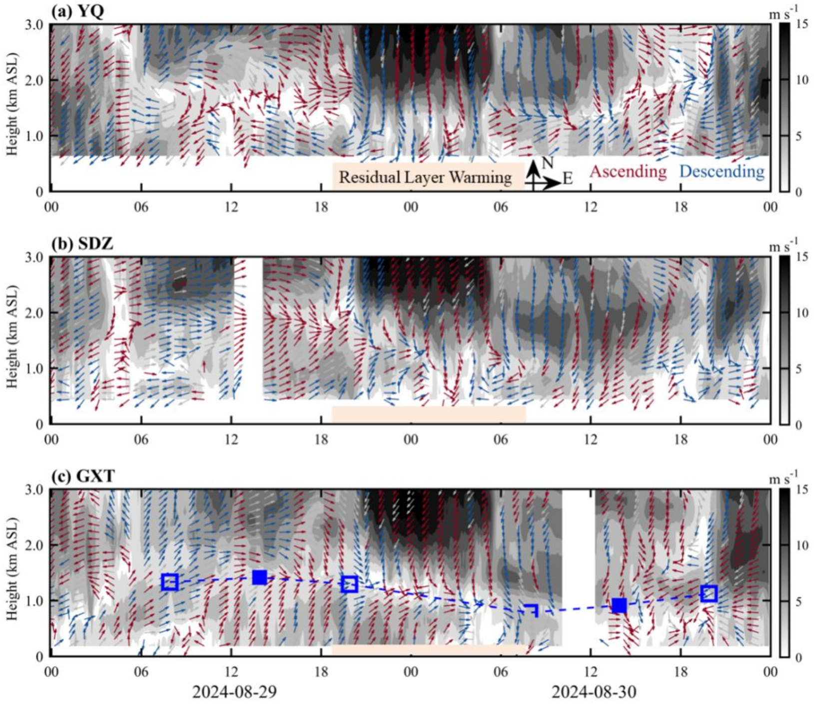

Figure 7. Radar-based wind profiles at the (a) YQ, (b) SDZ, and (c) GXT stations before, during, and after the elevated foehn-induced residual layer warming. Shaded areas represent horizontal wind speed; arrows denote horizontal wind direction (red indicates ascending motion, blue indicated descending motion). In (c), blue squares denote the convective boundary layer height (solid) or residual layer height (hollow); blue dashed line indicates the evolution of the convective boundary layer and residual layer heights.

3.1.3. Three-dimensional evolution of O_3 before, during, and after elevated foehn

The coordinated O_3 lidar observations at the urban (GXT) and rural (SDZ) stations provided a unique opportunity to elucidate the three-dimensional evolution of boundary-layer O_3 in response to elevated foehn. By integrating data from meteorological radiosondes and radar wind profilers, we investigated how sudden changes in boundary layer thermal and dynamical structure induced by elevated foehn affected O_3 evolution and quantified the differences in boundary layer O_3 transport fluxes between the pre- and post-foehn days (Fig. 8).

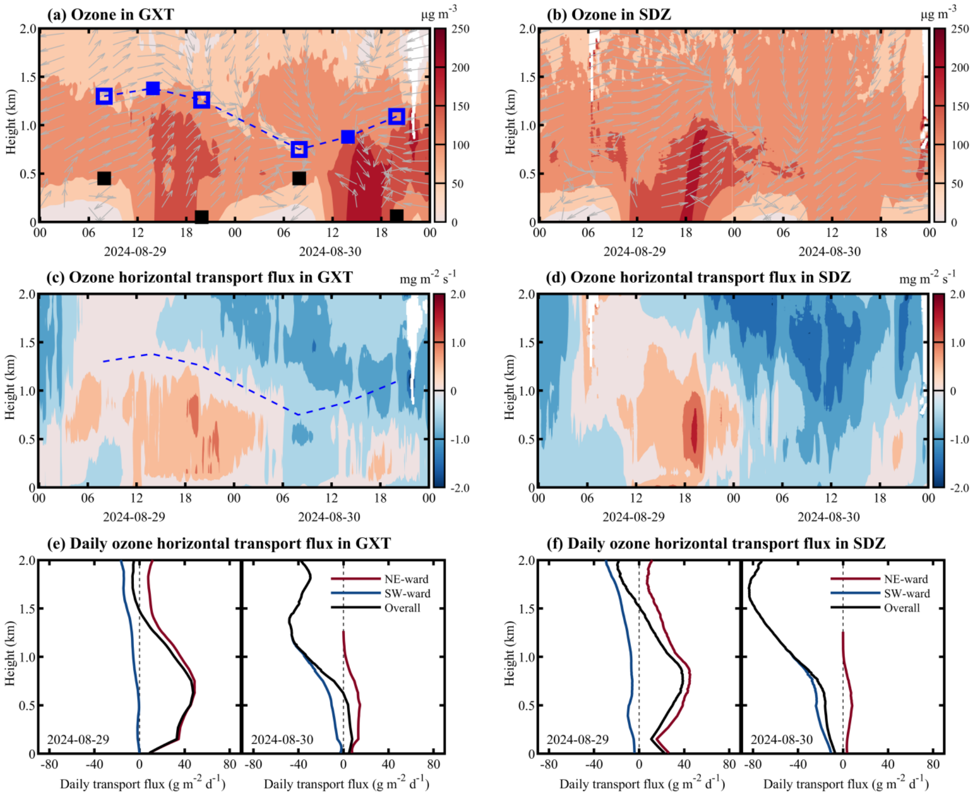

Figure 8. Vertical O_3 concentrations, wind direction, and O_3 transport flux at the GXT and SDZ stations. In (a), squares denote the boundary layer heights determined from radiosonde profiles (black for SBLH, blue for CBLH/RLH). The blue dashed line in (a) and (c) indicates the evolution of CBL and RL heights. In (c) and (d), positive (negative) horizontal transport flux indicates northeastward (southwestward) transport in the direction from GXT to SDZ. Panels (e) and (f) show the daily integrated O_3 transport flux at the GXT and SDZ stations on 29 and 30 August, respectively.

As shown in Fig. 8a, the boundary layer thermal structure critically shaped O_3 vertical distribution in urban Beijing: a steep gradient in the SBL, an O_3 reservoir in the RL, and relatively uniform mixing in the CBL. The elevated foehn-induced residual layer warming on the night of 29–30 August led to a significant reduction in the boundary layer height on 30 August, substantially compressing the vertical space for daytime O_3 mixing. Combined with enhanced photochemical O_3 production (due to higher temperatures) and weakened horizontal dispersion (due to lower post-foehn wind speeds,) these factors collectively contributed to a marked increase in afternoon boundary layer O_3 concentrations in urban Beijing on 30 August (200–250 μg m^{-3}) compared to the previous day (~150 μg m^{-3}). We also observed that the elevated foehn was accompanied by downward transport of free-tropospheric O_3 (Fig. 8a). However, due to the presence of a strong capping inversion acting as a transport barrier (Fig. 5), this descending free-tropospheric O_3 was unlikely to have significantly intruded into the boundary layer.

The urban-rural coordinated lidar observations clearly reveal a dynamically driven shift in spatial heterogeneity before and after the elevated foehn. On 29 August (pre-foehn), prevailing southwesterly flows facilitated the northeastward transport of the urban O_3 plume. The lidars recorded higher O_3 concentrations at the downwind rural SDZ station than at the urban GXT station (Fig. 8a and b). The peak O_3 occurrence at SDZ was delayed by 1–3 hours relative to GXT, consistent with advective transport. The calculated horizontal O_3 transport flux was predominantly northeastward in the boundary layer at both stations throughout the day, with stronger fluxes in the upper boundary layer. The instantaneous maximum flux at SDZ exceeded 2.0 mg m^{-3} s^{-1}, significantly higher than at GXT (Fig. 8c and d). In stark contrast, the post-foehn convergence stagnation on 30 August suppressed advective transport and promoted local O_3 accumulation in urban Beijing. Consequently, afternoon boundary layer O_3 concentrations at GXT reached notably high levels (200–250 μg m^{-3}), while concentrations at SDZ dropped to low values (~100 μg m^{-3}). Despite this spatial contrast, the boundary layer O_3 transport flux at both stations was markedly low compared to the previous day (Fig. 8c, d, e, and f), underscoring a shift in the dominant pollution mechanism from urban plume transport to urban pollution accumulation.

We examined the WRF-Chem output to gain further insight into the vertical O_3 structure over Beijing before and after the elevated foehn. As shown in Fig. 9, although the WRF-Chem model exhibited some deviations in simulating the boundary layer height, it successfully reproduced the pre-foehn northeastward transport of the urban O_3 plume on 29 August, as well as the post-foehn stagnation-driven local O_3 accumulation in the urban Beijing on 30 August. On 29 August, the O_3 pollution initially built up in the urban area (e.g., near GXT) by 11:00 BJT. By 14:00 BJT, the high-O_3 zone had shifted to the northern suburbs, and by 17:00 BJT, it had been transported to the rural areas in the northeast (e.g., near SDZ). In contrast, on 30 August, the relatively higher O_3 concentrations over Beijing were consistently confined in the urban area, with no significant spatial shift. These simulation results aligned well with the lidar observations. Furthermore, the WRF-Chem model reproduced the vertical wind patterns observed at GXT, SDZ, and YQ (Fig. 7), thereby better illustrating the vertical structure of the foehn flow during its decaying stage on 30 August via wind cross-sections. The foehn simulations show that while the near-surface component—shallow foehn—was blocked by prevailing southerly winds within the boundary layer, leading to convergence and airflow stagnation over urban Beijing, its upper-layer branch—elevated foehn—passed directly over the urban area unimpeded, resulting in persistent warming that suppressed the daytime convective boundary layer development until the foehn decayed around 14:00 BJT. These features are evident in both the GXT-YQ cross-section (parallel to the elevated northwesterly foehn) and the GXT-SDZ cross-section (perpendicular to the elevated northwesterly foehn). The configuration of an unimpeded elevated foehn and a blocked shallow foehn effectively explains the accumulation of higher O_3 concentrations in the urban boundary layer of Beijing on 30 August.

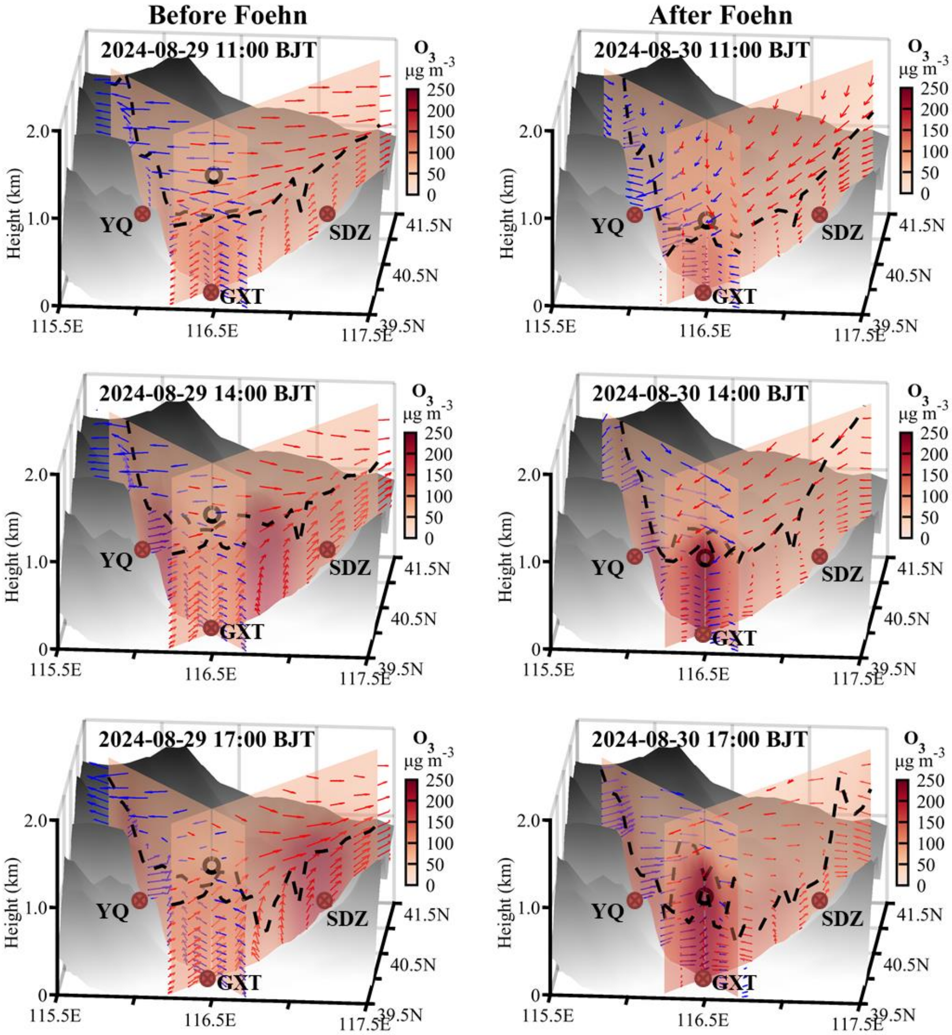

Figure 9. Cross-sections of simulated O_3 concentrations along the line across the GXT and SDZ stations and the line across GXT and YQ stations on 29 and 30 August. Dashed black lines denote the simulated boundary layer height, and arrows show the composite of simulated horizontal wind speed (m s^{-1}) and vertical wind speed (×10 m s^{-1}) in the GXT-SDZ (red arrows) and GXT-YQ (blue arrows) cross-sections. Only horizontal wind speed in the direction along the individual cross-sections is included. The black dots denote the boundary layer height observed at GXT and the height at 14:00 BJT is the observational value and these at 11:00 and 17:00 BJT are interpolated from two adjacent radiosonde observations.

3.2. Climatological evaluation

While a case study is valuable for mechanistic understanding, the question of representativeness always arises. To clarify whether the features identified in the case study are typical, we supplemented the case analysis with a climatological investigation of elevated foehn and its O_3 pollution effect based on long-term observations.

Based on summer radiosonde data from the GXT station during 2015-2024, we calculated overnight temperature change (ΔT_{12h}) profiles for each night by differencing the temperature profiles at 20:00 BJT and 08:00 BJT the following day. We identified a residual layer warming event when $\Delta T_{12h} > 3$ ℃ occurred within 500-2000 m height range. For each event, we identified the height of maximum warming and used it as the endpoint for backward trajectory calculations. Statistical results show that among the 920 valid summer observation days from 2015 to 2024, a total of 63 residual layer warming cases were identified, accounting for 6.85% of summer night. Figure 10 illustrates the ΔT_{12h} profiles, backward trajectories, and trajectory height/temperature changes for these events. While warming heights vary widely across different events, the composite ΔT_{12h} profile highlights warming above ~650 m, contrasting sharply with the summer mean profile showing nocturnal cooling throughout the layer. The backward trajectories of these warming air masses show that most originated from high-altitude regions to the west or north. After crossing the Yanshan or Taihang Mountains, these airflows arrived in Beijing, with their trajectories descending on average by 500 m and their temperature rising rapidly by an average of 10 ℃, exhibiting clear foehn characteristics. Applying the elevated foehn criteria from Sect. 2.2, 54 of the 63 warming cases (85.7%) can be attributed to elevated foehn. These results confirm that elevated foehn is the primary cause of nocturnal residual layer warming in Beijing.

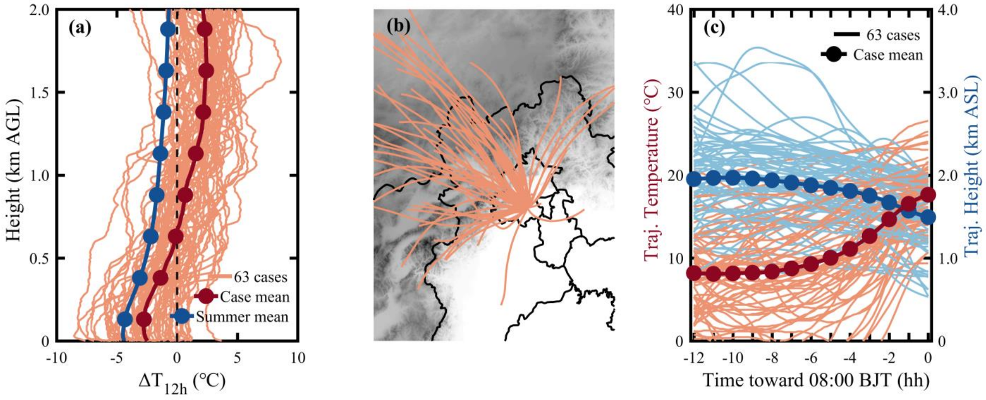

Figure 10. (a) Overnight temperature change (ΔT_{12h}) profiles from 20:00 BJT to next-day 08:00 BJT, (b) overnight airflow backward trajectories ending at the maximum warming height, and (c) overnight trajectory height and temperature changes for the 63 identified residual layer warming events.

Previous case analysis indicated that elevated foehn exacerbates next-day O_3 pollution through three pathways: increasing boundary layer temperature (enhancing photochemistry), reducing boundary layer height (inhibiting vertical diffusion), and weakening boundary layer winds (suppressing horizontal dispersion). Composite analyses of all 54 elevated foehn events (Fig. 11) strongly support the prevalence of these mechanisms. On average, post-foehn afternoon boundary layer temperature was more than 3 ℃ higher than pre-foehn conditions. The elevated foehn-induced residual layer warming directly led to an average RLH reduction of 480 m, and the subsequent afternoon CBLH was, on average, 110 m lower. Post-foehn afternoon boundary layer wind speed decreased by more than 1.0 $m\ s^{-1}$ on average. Overall, these meteorological changes consistently favor local O_3 production and accumulation. As a result, approximately 87 % of elevated foehn events were followed by worsened O_3 pollution. Post-foehn MDA8O_3 concentrations across Beijing increased by an average of 20–60% (varying by site) compared to the preceding day (Fig. 12b). Within the main urban zone (inside the 6th Ring Road), the

$MDA8O_3$ increase generally exceeded 45% (Fig. 12b), with concentrations commonly surpassing the national air quality standard of 160 μg m^{-3} (Fig. 12a).

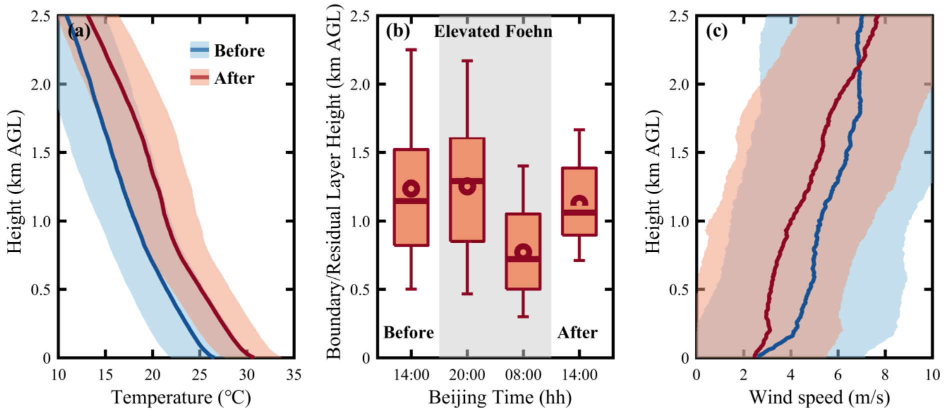

Figure 11. Composite of (a) afternoon boundary layer temperature profiles, (b) boundary/residual layer height, and (c) afternoon boundary layer wind speed profiles before, during, and after 54 identified elevated foehn events in Beijing. In (a) and (c), solid lines denote the mean profiles and shaded areas represent the standard deviation. In (b), box-and-whisker plots show the 5th, 25th, 50th, 75th, and 95th percentiles; dots represent the means.

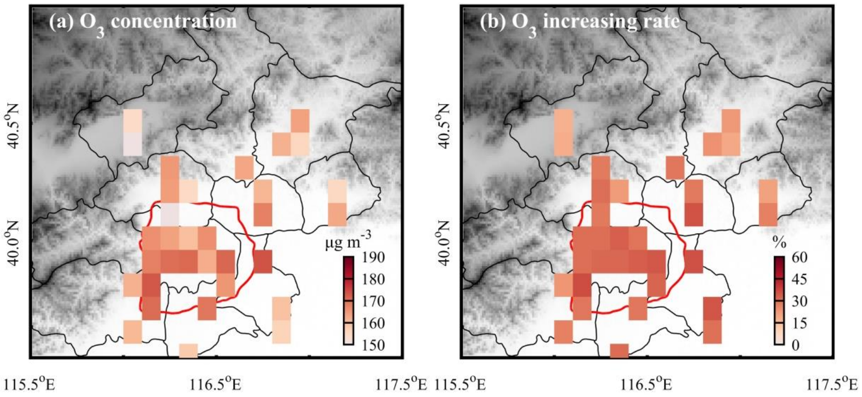

Figure 12. Composite of (a) daily maximum 8-h O_3 concentrations following elevated foehn in Beijing, and (b) their average percentage increase compared to preceding days. Note: site data are resampled and shown on a 0.1°×0.1° grid, accounting for the relocation of some sites around 2021.

4. Discussion

Traditionally, nocturnal warming has been considered rare. Previous studies have observed occasional nighttime surface warming in leeward plains or valleys due to foehn effects (Luo et al., 2020; Ma et al., 2015). This study, by creatively integrating radiosonde data, reveals for the first time the frequent occurrence of pronounced nocturnal residual layer warming in summer Beijing. The primary driver is identified as elevated foehn—an upper-layer phenomenon previously missed by near-surface observations. Theoretically, unlike near-surface warming from shallow foehn (which enhances boundary layer instability), residual layer warming from elevated foehn reinforces static stability (Stull, 1988). Our observations show that this warming substantially lowers the boundary layer

https://doi.org/10.5194/egusphere-2025-6492
Preprint. Discussion started: 23 March 2026

capping inversion (i.e., RLH), thereby inhibiting the development of the next day's convective boundary layer. While Pal and Lee (2019) highlighted that mountain air mass advection can lead to boundary layer overrunning over downwind plains, our results demonstrate that under elevated foehn, mountain-sourced air masses can instead act to lower the downwind boundary layer height through foehn warming.

The elevated foehn process in summer Beijing shows both similarities and differences with that in winter Urumqi (Li et al., 2015). The similarity lies mainly in the three-layer flow structure that causes similar "sandwich" foehn warming within a middle wind shear layer. The key difference lies in the post-foehn boundary layer convergence mechanism. In winter Urumqi, a downslope wind and hydraulic jump occur simultaneously on the northern leeside of the Tianshan Mountains after the foehn encounters a cold air pool in the southern suburbs, generating convergence between the cold pool and the shallow downslope wind (Li et al., 2015). In contrast, no such cold air pool exists in summer Beijing. Here, the post-foehn convergence instead results from the confrontation between the emerging northwestern foehn winds and the prevailing southwestern winds within the boundary layer.

Our results reveal that 86.9% of the identified elevated foehn events were followed by O_3 pollution exacerbation in summer Beijing. Post-foehn MDA8O_3 concentrations increased more than 30% on average, exceeding the national pollution threshold at most monitoring sites. In a previous study, Li et al. (2025) explored connections between ground-based foehn and $PM_{2.5}$ pollution in Beijing, finding that 60.4 % of cases corresponded to pollution mitigation and only 39.6% to exacerbation. While direct comparability is limited due to differences in pollutant ($PM_{2.5}$ vs. O_3) and season (annual vs. summer), the markedly higher probability of post-foehn pollution exacerbation found in our study clearly indicates that elevated foehn exhibits a more deterministic pollution effect. Therefore, elevated foehn can serve as a reliable meteorological precursor for O_3 pollution warnings in summer Beijing. Notably, since elevated foehn can be directly identified from routine radiosonde observations (Sect. 2.2), its application as a precursor for summer O_3 forecasting can be both highly convenient and timely.

5. Conclusion

This study systematically investigated the formation process of elevated foehn winds and their mechanisms for exacerbating surface O_3 pollution in summer Beijing through a combined case analysis and climatological evaluation. The main conclusions are as follows:

1、 First observational confirmation of elevated foehn events in summer Beijing. Utilizing high-resolution radiosonde observations, this study identified a novel phenomenon distinct from traditional near-surface foehn. It manifests as abnormal nocturnal warming ($\Delta T_{12h} > 3$ ℃) within the elevated residual layer (approximately 500–2000 m AGL), with no significant warming signal at the surface. Lagrangian back-trajectory analysis confirms that the warming air masses originate from the northwestern or northern plateaus, undergoing descent and warming after crossing the Yanshan or Taihang Mountains, exhibiting classic foehn characteristics. These elevated foehn events account for 5.87% of summer nights and are identified as the primary driver (85.7% of identified cases) of nocturnal residual layer warming in Beijing.

2、 Clarification of the triple synergistic mechanisms through which elevated foehn exacerbates next-day O_3 pollution. Thermodynamic Effect I: Increasing boundary layer temperature to enhance photochemical production. Nocturnal residual layer warming directly leads to a significantly higher daytime boundary layer temperature (average increase >3 ℃), accelerating the photochemical reaction rates of precursors. Thermodynamic Effect II: Lowering the boundary layer height to suppress vertical diffusion. The residual layer warming reinforces atmospheric stability, causing the capping inversion base (i.e., the residual layer height) to drop by an average of ~480 m and the subsequent afternoon convective boundary layer height to decrease by

~110 m. This substantially compresses the vertical mixing volume for pollutants. Dynamic Effect: Inducing boundary-layer convergent stagnation to weaken horizontal transport. The intruding northwesterly elevated foehn flow confronts the prevailing southwesterlies within the boundary layer, forming a convergence zone. This leads to a marked reduction in wind speed (average decrease >1.0 m s^{-1}), severely hindering the horizontal advective dispersion of pollutants.

3、 Decade-long climatological evaluation confirms the highly deterministic and prevalent exacerbating effect of elevated foehn on summer O_3 pollution. Composite analysis of 54 identified elevated foehn events from 2015–2024 robustly supports the proposed mechanisms. Statistics show that 87% of elevated foehn events were followed by worsened O_3 pollution the next day. The city-wide MDA8O_3 concentration increased by 20–60% on average compared to the preceding day, with increases in the main urban area typically exceeding 45%. Post-foehn MDA8O_3 concentrations commonly surpassed the national ambient air quality standard (160 μg m^{-3}). This stands in sharp contrast to previous statistics based on near-surface observations, which associate shallow foehn primarily with pollution alleviation (60.4% of cases), highlighting the fundamental difference in pollution potential between shallow and elevated foehn.

In summary, this study identifies elevated foehn as a significant and previously overlooked meteorological forcing factor for summer O_3 pollution in Beijing. Its synergistic "warming-lowering-stagnating" effects lead to a highly deterministic pollution exacerbation. Given that elevated foehn can be directly identified using routine radiosonde data, we propose its utility as a reliable and efficient meteorological precursor for O_3 pollution forecasting and warning in Beijing and other cities with similar topography. This provides a new scientific basis for the precise prevention and control of air pollution. Future research should focus on quantifying the contribution of elevated foehn to O_3 generation under different synoptic backgrounds and exploring its coupling with regional transport and chemical processes.

Data availability. The remote sensing observations and numerical simulation results are available from the correspondence author upon reasonable request (zqma@ium.cn).

Author contributions

Z.L. conceived the original idea, analyzed the data, and wrote the first version manuscript. J.X. conducted the WRF-Chem simulation. L.Z. operated the remote sensing equipment. C.L. performed the HYSPLIT model. Z.M. supervised the research project. All authors discussed the results and commented on the manuscript.

Competing interests

The authors declare no competing interests.

Acknowledgements

This research has been supported by the National Natural Science Foundation of China (Grant Nos. 42405115 and 42307150), and the Scientific Research Project of the Beijing Meteorological Bureau (Grant No. BMBKJ202404002). We acknowledge the DeepSeek for polishing our English language.

References

Baumann, K., Maurer, H., Rau, G., Piringer, M., Pechinger, U., Prévôt, A., Furger, M., Neininger, B., Pellegrini, U., 2001. The influence of south Foehn on the ozone distribution in the Alpine Rhine valley—results from the MAP field phase. Atmospheric Environment 35, 6379-6390.

Campana, M., Li, Y., Staehelin, J., Prevot, A.S.H., Bonasoni, P., Loetscher, H., Peter, T., 2005. The influence of south foehn on the ozone mixing ratios at the high alpine site Arosa. Atmospheric Environment 39, 2945-2955.

Elvidge, A.D., Renfrew, I.A., 2016. The Causes of Foehn Warming in the Lee of Mountains. Bulletin of the American Meteorological Society 97, 455-466.

Gaffin, D.M., 2002. Unexpected Warming Induced by Foehn Winds in the Lee of the Smoky Mountains. Weather and Forecasting 17, 907-915.

Gaffin, D.M., 2009. On High Winds and Foehn Warming Associated with Mountain-Wave Events in the Western Foothills of the Southern Appalachian Mountains. Weather and Forecasting 24, 53-75.

Grell, G.A., Peckham, S.E., Schmitz, R., McKeen, S.A., Frost, G., Skamarock, W.C., Eder, B., 2005. Fully coupled "online" chemistry within the WRF model. Atmospheric Environment 39, 6957-6975.

Gu, Y., Li, K., Xu, J., Liao, H., Zhou, G., 2020. Observed dependence of surface ozone on increasing temperature in Shanghai, China. Atmospheric Environment 221, 117108.

Guenther, A., Karl, T., Harley, P., Wiedinmyer, C., Palmer, P.I., Geron, C., 2006. Estimates of global terrestrial isoprene emissions using MEGAN (Model of Emissions of Gases and Aerosols from Nature). Atmos. Chem. Phys. 6, 3181-3210.

Kerr, R.A., 1986. Chinook Winds Resemble Water Flowing over a Rock. Science 231, 1244-1245.

Kirchgaessner, A., King, J.C., Anderson, P.S., 2021. The Impact of Föhn Conditions Across the Antarctic Peninsula on Local Meteorology Based on AWS Measurements. Journal of Geophysical Research: Atmospheres 126, e2020JD033748.

Li, J., Sun, Z., Lenschow, D.H., Zhou, M., Dou, Y., Cheng, Z., Wang, Y., Li, Q., 2020a. A foehn-induced haze front in Beijing: observations and implications. Atmos. Chem. Phys. 20, 15793-15809.

Li, J., Zhang, J., Bai, M., Su, J., Li, Q., Jia, X., 2025. Identification and characterization of foehn events in Beijing and their impact on air pollution episodes. Atmos. Chem. Phys. 25, 8683-8700.

Li, X., Xia, X., Wang, L., Cai, R., Zhao, L., Feng, Z., Ren, Q., Zhao, K., 2015. The role of foehn in the formation of heavy air pollution events in Urumqi, China. Journal of Geophysical Research: Atmospheres 120, 5371-5384.

Li, X., Xia, X., Zhong, S., Luo, L., Yu, X., Jia, J., Zhao, K., Li, N., Liu, Y., Ren, Q., 2020b. Shallow foehn on the northern leeside of Tianshan Mountains and its influence on atmospheric boundary layer over Urumqi, China — A climatological study. Atmospheric Research 240, 104940.

Li, Y., Chen, M., Miao, S., Zhang, G., Huang, Q., Zhang, S., 2026. Evaluation of three scale-aware planetary boundary layer schemes in WRF Model during Beijing 2022 Winter Olympics. Atmospheric Research 328, 108416.

Liao, Z., Pan, Y., Ma, P., Jia, X., Cheng, Z., Wang, Q., Dou, Y., Zhao, X., Zhang, J., Quan, J., 2023. Meteorological and chemical controls on surface ozone diurnal variability in Beijing: A clustering-based perspective. Atmospheric Environment 295, 119566.

Liao, Z., Sun, J., Yao, J., Liu, L., Li, H., Liu, J., Xie, J., Wu, D., Fan, S., 2018. Self-organized classification of boundary layer meteorology and associated characteristics of air quality in Beijing. Atmos. Chem. Phys. 18, 6771-6783.

Liu, S., Liang, X.-Z., 2010. Observed Diurnal Cycle Climatology of Planetary Boundary Layer Height. Journal of Climate 23, 5790-5809.

Luo, R., Zheng, Y., Chen, M., 2020. Mechanism of a rare night sudden intense warming event in Beijing and surrounding area. Meteorol. Monthly (in Chinese) 46, 478-489.

Ma, Y., Yang, Y., Hu, X., Gan, R., 2015. Characteristics and Mechanisms of the Sudden Warming Events in the Nocturnal Atmospheric Boundary Layer: A Case Study Using WRF. Journal of Meteorological Research 29, 747-763.

Miltenberger, A.K., Reynolds, S., Sprenger, M., 2016. Revisiting the latent heating contribution to foehn warming: Lagrangian analysis of two foehn events over the Swiss Alps. Quarterly Journal of the Royal Meteorological Society 142, 2194-2204.

Ouyang, S., Deng, T., Liu, R., Chen, J., He, G., Leung, J.C.H., Wang, N., Liu, S.C., 2022. Impact of a subtropical high and a typhoon on a severe ozone pollution episode in the Pearl River Delta, China. Atmos. Chem. Phys. 22, 10751-10767.

Pal, S., Lee, T.R., 2019. Advected Air Mass Reservoirs in the Downwind of Mountains and Their Roles in Overrunning Boundary Layer Depths Over the Plains. Geophysical Research Letters 46, 10140-10149.

Seibert, P., Feldmann, H., Neininger, B., Bäumle, M., Trickl, T., 2000. South foehn and ozone in the Eastern Alps – case study and climatological aspects. Atmospheric Environment 34, 1379-1394.

Shu, L., Xie, M., Wang, T., Gao, D., Chen, P., Han, Y., Li, S., Zhuang, B., Li, M., 2016. Integrated studies of a regional ozone pollution synthetically affected by subtropical high and typhoon system in the Yangtze River Delta region, China. Atmos. Chem. Phys. 16, 15801-15819.

Stein, A.F., Draxler, R.R., Rolph, G.D., Stunder, B.J.B., Cohen, M.D., Ngan, F., 2015. NOAA's HYSPLIT Atmospheric Transport and Dispersion Modeling System. Bulletin of the American Meteorological Society 96, 2059-2077.

Steinhoff, D.F., Bromwich, D.H., Speirs, J.C., McGowan, H.A., Monaghan, A.J., 2014. Austral summer foehn winds over the McMurdo dry valleys of Antarctica from Polar WRF. Quarterly Journal of the Royal Meteorological Society 140, 1825-1837.

Stull, R.B., 1988. An Introduction to Boundary Layer Meteorology; Kluwer Academic Publishers, Dordrecht, The Netherlands.

Tang, G., Zhang, J., Zhu, X., Song, T., Münkel, C., Hu, B., Schäfer, K., Liu, Z., Zhang, J., Wang, L., Xin, J., Suppan, P., Wang, Y., 2016. Mixing layer height and its implications for air pollution over Beijing, China. Atmos. Chem. Phys. 16, 2459-2475.

Wang, X.Y., Wang, K.C., 2014. Estimation of atmospheric mixing layer height from radiosonde data. Atmos. Meas. Tech. 7, 1701-1709.

Xu, J., Zhang, Z., Zhao, X., Zhang, J., 2024. Synthetically impacts of the topography and typhoon periphery on the atmospheric boundary layer structure and special regional pollution pattern of O3 in North China Plain. Atmospheric Environment 330, 120566.

Yang, X., Yang, M., Li, J., Zhang, S., 2018. Impact analysis of a Taihang Mountain foehn on haze intensity. Meteorol. Monthly (in Chinese) 44, 313-319.

Zhang, Q., Streets, D.G., Carmichael, G.R., He, K.B., Huo, H., Kannari, A., Klimont, Z., Park, I.S., Reddy, S., Fu, J.S., Chen, D., Duan, L., Lei, Y., Wang, L.T., Yao, Z.L., 2009. Asian emissions in 2006 for the NASA INTEX-B mission. Atmos. Chem. Phys. 9, 5131-5153.

Zhang, S., Zeng, G., Yang, X., Wu, R., Yin, Z., 2021. Comparison of the influence of two types of cold surge on haze dispersion in eastern China. Atmos. Chem. Phys. 21, 15185-15197.

Zong, L., Yang, Y., Xia, H., Yuan, J., Guo, M., 2023. Elucidating the Impacts of Various Atmospheric Ventilation Conditions on Local and Transboundary Ozone Pollution Patterns: A Case Study of Beijing, China. Journal of Geophysical Research: Atmospheres 128, e2023JD039141.